






# Chronic acidosis rewires cancer cell metabolism through PPAR $\alpha$ signaling

Michala G. Rolver<sup>1</sup>  | Lya K. K. Holland<sup>2</sup> | Muthulakshmi Ponniah<sup>1</sup> |  
 Nanditha S. Prasad<sup>1</sup> | Jiayi Yao<sup>3,4</sup> | Julie Schnipper<sup>5</sup> | Signe Kramer<sup>1</sup> |  
 Line Elingaard-Larsen<sup>6</sup> | Elena Pedraz-Cuesta<sup>1</sup> | Bin Liu<sup>2</sup> | Luis A. Pardo<sup>7</sup> |  
 Kenji Maeda<sup>2</sup> | Albin Sandelin<sup>3,4</sup>   | Stine Falsig Pedersen<sup>1</sup>  

<sup>1</sup>Section for Cell Biology and Physiology, Department of Biology, University of Copenhagen, Copenhagen, Denmark

<sup>2</sup>Cell Death and Metabolism, Center for Autophagy, Recycling and Disease, Danish Cancer Society Research Center, Copenhagen, Denmark

<sup>3</sup>The Bioinformatics Center, Department of Biology, University of Copenhagen, Copenhagen, Denmark

<sup>4</sup>Biotech Research and Innovation Center, University of Copenhagen, Copenhagen, Denmark

<sup>5</sup>Laboratory of Cellular and Molecular Physiology, University of Picardie Jules Verne, Amiens, France

<sup>6</sup>Department of Clinical Research, Steno Diabetes Center Copenhagen, Herlev, Denmark

<sup>7</sup>Oncophysiology Group, Max-Planck-Institute for Multidisciplinary Sciences, Göttingen, Germany

## Correspondence

Stine Falsig Pedersen and Michala G. Rolver,  
 Section for Cell Biology and Physiology,  
 Department of Biology, University of  
 Copenhagen, Denmark.  
 Email: [sfpedersen@bio.ku.dk](mailto:sfpedersen@bio.ku.dk) and [michala.rolver@bio.ku.dk](mailto:michala.rolver@bio.ku.dk)

Albin Sandelin, The Bioinformatics Centre,  
 Department of Biology, University of  
 Copenhagen, Denmark.  
 Email: [albin@binf.ku.dk](mailto:albin@binf.ku.dk)

## Funding information

Danish Cancer Society, Grant/Award  
 Numbers: A12359, R124-A7929-15-S2;  
 Department of Biology, University of  
 Copenhagen, Grant/Award Number: BIO Elite  
 PhD Scholarship; Independent Research Fund  
 Denmark, Grant/Award Numbers: 6108-  
 00542B, 0135-00139B; Novo Nordisk  
 Fonden, Grant/Award Number:  
 NNF19OC0058262

## Abstract

The mechanisms linking tumor microenvironment acidosis to disease progression are not understood. Here, we used mammary, pancreatic, and colon cancer cells to show that adaptation to growth at an extracellular pH (pH<sub>e</sub>) mimicking acidic tumor niches is associated with upregulated net acid extrusion capacity and elevated intracellular pH at physiological pH<sub>e</sub>, but not at acidic pH<sub>e</sub>. Using metabolic profiling, shotgun lipidomics, imaging and biochemical analyses, we show that the acid adaptation-induced phenotype is characterized by a shift toward oxidative metabolism, increased lipid droplet-, triacylglycerol-, peroxisome content and mitochondrial hyperfusion. Peroxisome proliferator-activated receptor- $\alpha$  (PPARA, PPAR $\alpha$ ) expression and activity are upregulated, at least in part by increased fatty acid uptake. PPAR $\alpha$  upregulates genes driving increased mitochondrial and peroxisomal mass and  $\beta$ -oxidation capacity, including mitochondrial lipid import proteins CPT1A, CPT2 and SLC25A20, electron transport chain components, peroxisomal proteins PEX11A and ACOX1, and thioredoxin-interacting protein (TXNIP), a negative regulator of glycolysis. This endows acid-adapted cancer cells with increased capacity for utilizing fatty acids for

**Abbreviations:** ECAR, extracellular acidification rate; GPL, glycerophospholipid; LD, lipid droplet; MCT, monocarboxylate transporter; NBCn1, electroneutral Na<sup>+</sup>, HCO<sub>3</sub><sup>-</sup> cotransporter-1; NHE1, Na<sup>+</sup>/H<sup>+</sup> exchanger-1; OCR, oxygen consumption rate; ORO, Oil-Red-O; PDAC, pancreatic ductal adenocarcinoma; pH<sub>e</sub>, extracellular pH; pH<sub>i</sub>, intracellular pH; PPAR $\alpha$ , peroxisome proliferator-activated receptor- $\alpha$ ; PPRE, peroxisome proliferator response element; TAG, triacylglycerol; TME, tumor microenvironment; TXNIP, thioredoxin-interacting protein; V-ATPase, V-type H<sup>+</sup> ATPase; VLCFA, very-long chain fatty acid.

Michala G. Rolver, Lya K. K. Holland and Muthulakshmi Ponniah have contributed equally to this study.

This is an open access article under the terms of the [Creative Commons Attribution-NonCommercial-NoDerivs](https://creativecommons.org/licenses/by-nc-nd/4.0/) License, which permits use and distribution in any medium, provided the original work is properly cited, the use is non-commercial and no modifications or adaptations are made.

© 2022 The Authors. *International Journal of Cancer* published by John Wiley & Sons Ltd on behalf of UICC.

metabolic needs, while limiting glycolysis. As a consequence, the acid-adapted cells exhibit increased sensitivity to PPAR $\alpha$  inhibition. We conclude that PPAR $\alpha$  is a key upstream regulator of metabolic changes favoring cancer cell survival in acidic tumor niches.

#### KEYWORDS

acidic microenvironment, cancer metabolism, fatty acid metabolism, PPAR $\alpha$ ,  $\beta$ -oxidation

#### What's new?

The microenvironment of solid tumors contains highly acidic niches proposed to favor cancer aggressiveness, but the mechanisms involved are not understood. Here we show that cancer cells adapted to tumor acidosis exhibit increased metabolic flexibility, peroxisome- and mitochondria content, and lipid metabolism. We demonstrate that these changes are driven at least in part by increased PPAR $\alpha$  activity. Importantly, this renders acid-adapted cancer cells sensitive to PPAR $\alpha$  inhibition, pointing to a therapeutic relevance of targeting PPAR $\alpha$ .

## 1 | INTRODUCTION

Extracellular acidosis is a key feature of the tumor microenvironment (TME), resulting from the high metabolic activity of rapidly proliferating cancer cells and limited venting of metabolic waste products due to poor vascularization.<sup>1-3</sup> Metabolic acid production comprises both H<sup>+</sup> from glycolysis and CO<sub>2</sub> from oxidative phosphorylation (OXPHOS) and can thus be extensive in oxidative as well as hypoxic tumor regions. Consequently, acidosis and hypoxia only partially overlap.<sup>4,5</sup>

Recent studies have shown that adaptation to chronic extracellular acidosis can contribute to tumor aggressiveness, leading to the hypothesis that the acidic TME may, similar to hypoxia, play a key role in tumor development. For example, growth at acidic extracellular pH (pH<sub>e</sub>) favors epithelial-to-mesenchymal transition, invasiveness and metastasis in several cancer cell types,<sup>6-9</sup> and treatments limiting tumor acidosis attenuate cancer development and metastasis.<sup>10</sup> In contrast, effects of acid adaptation on cancer cell growth and proliferation have received less attention. Where this has been addressed, growth rates of acid-adapted cells were found to be similar to, or lower, than those of cells grown at normal tissue pH<sub>e</sub>.<sup>7,9</sup> Given that even modest acidification of intracellular pH (pH<sub>i</sub>) inhibits cell cycle progression, protein synthesis and hence cell growth,<sup>11-14</sup> this raises the question of how pH<sub>i</sub> is regulated in acid-adapted cancer cells. At the acidic pH<sub>e</sub> of the TME, cancer cell pH<sub>i</sub> is highly challenged given the strong inward-directed driving force for H<sup>+</sup>.<sup>15</sup> Cancer cells can restore a pH<sub>i</sub> compatible with proliferation in an acidic environment in two, not mutually exclusive, ways: (i) upregulate expression and/or activity of net acid-extruding mechanisms such as Na<sup>+</sup>/H<sup>+</sup> exchangers, Na<sup>+</sup>-HCO<sub>3</sub><sup>-</sup> cotransporters, V-type H<sup>+</sup> ATPases, or monocarboxylate transporters, and/or (ii) reduce metabolic acid production. Upregulation of net acid-extruding transporters in cancer cells and tumor tissue compared with normal cells/tissue has been reported by many studies,<sup>16-18</sup> but the regulation of such transporters in chronic acidosis is essentially unstudied.

Consistent with the extensive glycolysis-inhibitory effect of acidic pH<sub>i</sub>,<sup>19</sup> acid adaptation in cancer cells is associated with a metabolic shift away from glycolysis toward glutamine metabolism and fatty acid oxidation.<sup>20-23</sup> This is presumably because, at least initially, the only cells that survive are those that are able to adapt their metabolism to pathways that are operational at a more acidic pH. Only a few pathways that may regulate cancer cell metabolic rewiring by chronic acidosis are reported. These include transforming growth factor beta-2 (TGF- $\beta$ 2), which was assigned a role as a driver of lipid droplet (LD) accumulation in chronic acidosis<sup>20</sup>; and Thioredoxin-interacting protein (TXNIP), suggested to regulate glucose metabolism, downstream from transcription factor MondoA (MLXIP) in cancer cells subjected to acidic growth.<sup>24</sup> Thus, despite their importance for cancers *in vivo*, the adaptive changes in acid-base homeostasis and metabolism occurring in cancer cells during extended growth at acidic pH<sub>e</sub> are currently not understood.

We recently undertook deep RNA sequencing of three acid-adapted human cancer cell lines: Panc-1 pancreatic cancer cells, and MCF-7 (luminal B) and MDA-MB-231 (triple negative) breast cancer cells. This revealed a clear correlation between the acid adaptation gene expression response and gene expression changes between normal and tumor patient tissue across multiple cancers,<sup>25</sup> emphasizing that responses induced by chronic extracellular acidosis are likely to be relevant to tumor development in patients.

Here we ask which mechanisms allow cancer cell growth under the pressure of a strong inward-directed H<sup>+</sup> gradient in the acidic TME. We demonstrate that adaptation to growth at acidic pH upregulates net acid extrusion capacity, leading to elevated cancer cell pH<sub>i</sub> at physiological pH<sub>e</sub>, but not at acidic pH<sub>e</sub>. This is paralleled by extensive metabolic changes, including a shift toward oxidative metabolism, lipid uptake and increased peroxisome proliferator-activated receptor- $\alpha$  (PPARA, PPAR $\alpha$ ) activity. PPAR $\alpha$  drives the upregulation of genes required for increased mitochondrial and peroxisomal mass and fatty acid  $\beta$ -oxidation capacity, allowing the cells to utilize the fatty acids for their metabolic needs and increasing their sensitivity to PPAR $\alpha$  inhibition.

## 2 | MATERIALS AND METHODS

Additional methods details are provided in the online Supplement.

### 2.1 | Antibodies and reagents

Antibodies and primer sequences are provided in Tables S1 and S2, respectively. PPAR $\alpha$  antagonist (GW6471, #G5045), PPAR $\alpha$  agonist (GW7647, #G6793) and PPAR $\gamma$  antagonist (GW9662, #G6191) were from Sigma; and Hoechst (#33342) and Rhodamine Phalloidin (#A12379) from Thermo Fischer Scientific. Horseradish peroxidase (HRP)-conjugated secondary antibodies were from DAKO (#P0447, #P0448), and Alexa Fluor488 and – 568-conjugated secondary antibodies for immunofluorescence (IF) analysis were from Invitrogen (#A11019, # A11070).

### 2.2 | Cell lines and cell culture

All experiments were performed with mycoplasma-free cells. All cell lines were authenticated by STR profiling within the last 3 years. Panc-1 (RRID: CVCL\_0480), MDA-MB-231 (RRID: CVCL\_0062) (both ATCC), MCF-7/S9 (RRID: CVCL\_AS09) (gift from L. Rønnov-Jessen, University of Copenhagen) and HCT116 (RRID: CVCL\_0291) cells were cultured in RPMI-1640 (Sigma-Aldrich, R1383) with 10 mM glucose (Sigma-Aldrich, G8644), 5% fetal bovine serum (Sigma-Aldrich, F9665) and 1% Penicillin/Streptomycin (Sigma-Aldrich, #P0781). To adjust pH to 7.6, 7.4 or 6.5, 38, 24 or 3 mM NaHCO $_3^-$  and 0, 14 or 35 mM NaCl, respectively, was added to the medium. Cells were adapted to pH 7.6 or 6.5 by maintaining them in appropriately pH-adjusted medium for at least 4 weeks. Cells were cultured at 37°C, 5% CO $_2$ , passaged at ~70% to 80% confluence, and discarded after passage 23.

### 2.3 | BrdU proliferation assay

$3 \times 10^3$  cells were seeded and incubated for 24 h at 37°C, 5% CO $_2$  prior to adding the BrdU labeling reagent (1:100, Roche, #11647229001). After 4 h, cells were fixed and denatured for 30 min at room temperature (RT), incubated with BrdU antibody (Roche, #11647229001) according to the manufacturer's protocol. BrdU incorporation was measured colorimetrically in a BMG FLUOstar OPTIMA microplate reader (BMG Labtech, Ortenburg, Germany).

### 2.4 | Western blotting

Briefly, cells were grown to 70% to 80% confluence, lysed, diluted in NuPAGE LDS  $\times 4$  sample buffer and separated on 10% Criterion TGX Precast gels using Tris/Glycine/SDS running buffer. Proteins were transferred to nitrocellulose membranes, blocked in 5% nonfat dry milk or 5% BSA in TBST for 1 h at 37°C and incubated with primary

antibodies overnight at 4°C. The following day, membranes were incubated with secondary antibodies for 1 h at RT and developed using ECL or SignalFire on a Fusion FX developer (Vilber Lourmat). Band intensity was quantified using ImageJ software. For further details, see supplementary methods.

### 2.5 | Live imaging of intracellular pH (pH $_i$ )

Cells were seeded in WillCo wells (#HBST-3522), incubated at 37°C, 5% CO $_2$  to 70-80% confluence, incubated for 30 min with 1.6  $\mu$ M 2',7'-bis-(2-carboxyethyl)-5-(and-6)-carboxyfluorescein acetoxymethyl ester (BCECF-AM), washed in the appropriate HCO $_3^-$ -containing Ringer, and placed in a 37°C/5% CO $_2$ /air chamber with solute perfusion on a Nikon Eclipse Ti microscope. Fluorescence was measured ratiometrically (excitation: 440/485 nm; emission: 520 nm, EasyRatio-Pro software, PTI), for ~10 min in the appropriate HCO $_3^-$ -Ringer. Ringer composition (in mM for the pH 7.4 Ringer): 119 NaCl, 24 NaHCO $_3$ , 5 KCl, 0.83 MgSO $_4$ , 2 Na $_2$ HPO $_4$ , 2 CaCl $_2$ , 3.3 3-(N-morpholino)propanesulfonic acid (MOPS), 3.3 2-[Tris(hydroxymethyl)-methylamino]-ethanesulfonic acid (TES), 5 HEPES. Ringer NaHCO $_3$  and NaCl concentrations were adjusted to pH 7.6, 7.4 or 6.5 while maintaining [Na $^+$ ]. Linear pH $_i$  calibration was performed using high KCl Ringers (pH 6.6, 7.0, 7.4, 7.8) and 5  $\mu$ M nigericin, as in Reference 26.

### 2.6 | Immunofluorescence (IF) analysis

Briefly, cells seeded on coverslips were fixed with 2% paraformaldehyde, permeabilized in 0.5% Triton-X-100, blocked in 5% BSA in TBST, and incubated with primary antibodies in 1% BSA in TBST for 1.5 h/ON at RT/4°C. Hereafter, coverslips were incubated with secondary antibodies, and if indicated, Rhodamine-phalloidin, in 1% BSA in TBST, counterstained with DAPI, mounted in N-propylgallate mounting medium, and imaged using an Olympus IX83 microscope with a Yokogawa scanning unit. No image processing except merges, zooms and color balance was performed. Image quantifications, overlays and adjustments of the intensities were performed using ImageJ software (for details, see supplementary methods).

### 2.7 | RNA-seq analysis

Mapped RNA-seq data was retrieved from GEO (accession number GSE152345).<sup>25</sup> Differential expression analyses were performed individually for each cell line (AA vs ctrl.). Voom transformation was applied with a design matrix that used pH treatment as coefficient, and was then put into the linear model fit using Limma R package.<sup>27</sup> Differential expression, given the above settings, was defined as Benjamini-Hochberg FDR < 0.05. GSEA analysis is described in Supplementary Methods.

## 2.8 | Glycolytic stress test

Cells seeded in 96-well plates were incubated with XF base medium with 2 mM glutamine for 1 h at 37°C, no CO<sub>2</sub>, loaded into the Seahorse XFe96 Extracellular Flux Analyzer, and glucose, oligomycin and 2-deoxy-glucose were injected at final concentrations of 10 mM, 1 μM and 50 mM, respectively. Extracellular acidification and oxygen consumption rates (ECAR and OCR) were measured using 3 cycles of 3 min of mixing followed by three measurements over a period of ~18 min. Nuclei were stained with Hoechst (1:1000) and data normalized to cell count (for details, see supplementary methods).

## 2.9 | Mitochondrial analyses

### 2.9.1 | Quantification

Cells seeded in 96-well plates were stained for 30 min with MitoTracker Green FM (200 nM) and Hoechst, washed twice in PBS, and recorded in a GloMax Discover Microplate reader (Promega). The MitoTracker/Hoechst signal ratio was calculated per well (triplicates), and data are shown as mean per experiment, with SEM error bars (for details, see supplementary methods).

### 2.9.2 | Morphology

Cells seeded in Ibidi 4-well μ-slides were stained with MitoTracker Deep Red (100 nM) and Hoechst for 10 min at 37°C in Live Cell Imaging Solution pH 6.5, 7.4, or 7.6, washed once in this solution and imaged under temperature- and humidity-control, using an Nikon-Andor spinning disk confocal microscope and a 100X objective. Data were analyzed using Fiji software.

## 2.10 | Oil-Red-O staining

Cells grown on coverslips were washed with PBS and fixed with 4% PFA for 1 h at RT. Cells were stained for 15 min at RT with a filtered (0.2 μm) 0.5% Oil-Red-O solution (ORO, Sigma #00625, dissolved in 99% isopropanol, diluted 3:2 with ddH<sub>2</sub>O), washed with PBS, stained with DAPI (1:1000) and mounted as above. ORO-stained lipid droplets were visualized employing an Olympus IX83 microscope with a Yokogawa scanning unit, ×60/1.4 NA oil immersion objective and CellSens Dimension software. Quantification, image overlays, zooms and color balance adjustments were performed in ImageJ software.

## 2.11 | Shotgun lipidomics

Approximately  $1 \times 10^6$  cells were washed three times with 1 ml ice-cold 155 mM NH<sub>4</sub>HCO<sub>3</sub> in H<sub>2</sub>O. Then,  $2 \times 10^5$  of the washed cells were, together with a series of added internal lipid standards,

subjected to total lipid extraction and quantitative mass spectrometry-based lipidomics as in Reference 28. The molar quantities of identified lipid species and lipid classes in samples were determined and normalized to that of the total identified lipids (mol%) (Tables S5 and S6) (TAG was excluded from the normalization of the other lipid classes).

## 2.12 | Transcription factor binding site analysis

Upregulated genes based on the RNA-seq data analysis (FDR < 0.05, AA vs ctrl.) in MDA-MB-231 or Panc-1 cells were used as input in the oPOSSUM tool<sup>29</sup> with standard settings (±5kbp regions around transcription start sites of the above genes; JASPAR<sup>30</sup> sequence motifs). We sorted over-represented sequence motifs by opossium Fisher scores, and selected the union of the 15 most over-represented motifs in any of the two cells. For expression analysis of genes corresponding to motifs, we used mouse or human gene names corresponding to motif names.

## 2.13 | Quantitative real-time PCR (qPCR)

Total RNA was isolated using NucleoSpin RNA II (Macherey-Nagel) and reverse-transcribed using Superscript III Transcriptase (Invitrogen, #18080044). cDNA was amplified in triplicates by qPCR utilizing SYBR Green (Roche, #04913914001) in an ABI7900 qPCR machine with the steps: 95°C for 10 min, 40 × [95°C for 30 s, 55-63°C (depending on the primer pair) for 1 min, 72°C for 30 s], 95°C for 1 min. Primers were designed using NCBI Primer-BLAST, synthesized by Eurofins and diluted in nuclease-free H<sub>2</sub>O (2 μM working dilution). mRNA levels were determined using the Pfaffl method, normalized to β-actin and TATA-binding protein (TBP), and expressed relative to the mRNA level in ctrl. cells.

## 2.14 | PPARα and -γ agonist and antagonist treatment

For experiments involving treatments with the PPARα agonist and the PPARα and PPARγ antagonists, cells were seeded for the relevant experiment at least 24 h prior to treatment and treated with the indicated concentrations for either 24 or 72 h. All compounds were dissolved in DMSO.

## 2.15 | Dual luciferase assay

Cells in 6-well plates at 50% to 70% confluence were transfected with 1 μg/well PPRE X3-TK Luc plasmid (Addgene #1015) and 0.3 μg pRL-TK (Promega) employing Lipofectamine 3000 (Invitrogen, #L3000015). After 4 to 5 h, medium was exchanged and after 48 h, lysates were acquired with Passive Lysis Buffer (Promega, #E1910)

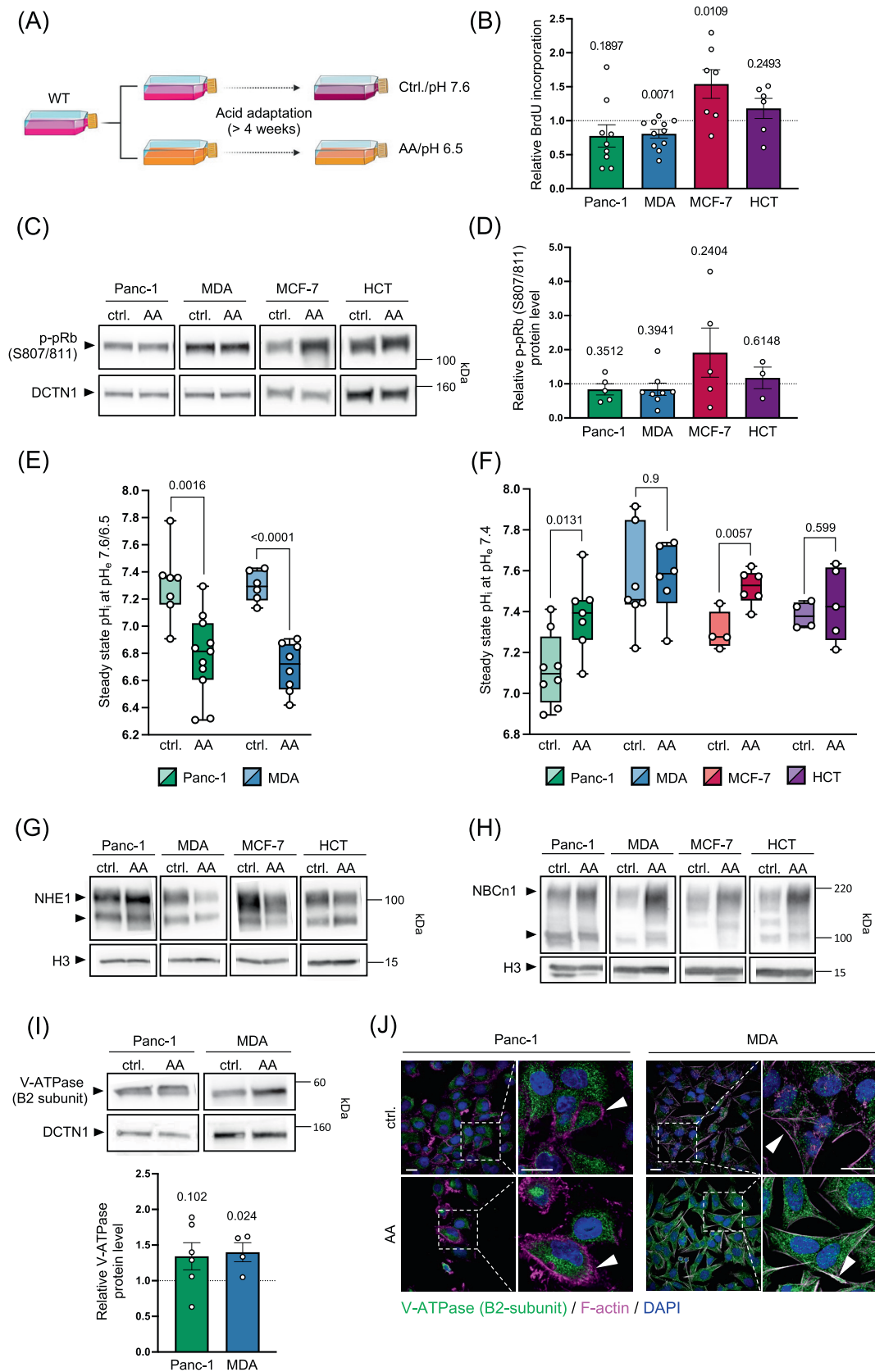


**FIGURE 1** Legend on next page.

diluted in ddH<sub>2</sub>O and luciferase activity assessed by Dual Luciferase Reporter Assay (Promega, #E1910) in a FLUOstar OPTIMA microplate reader (BMG Labtech, Ortenburg, Germany). Results are shown as fold increase in Firefly luciferase signal after background subtraction and normalization to pRL-TK Renilla luciferase signal. Where indicated, cells were treated for 24 h with GW7647 or GW6471 24 h after transfection.

### 2.16 | Cell viability assay

2 × 10<sup>3</sup> cells were plated in black-walled 96-well plates (Greiner-Bio, #655097) and grown for 24 h before being treated with either GW6471 or GW9662 at the indicated doses for 72 h. To evaluate cell viability, the medium was replaced with PBS and 50 µl CellTiter Glo 3D Reagent (Promega, #G9683) was added. Plates were shaken for 5 min, incubated for 25 min at RT and the luminescent signal was recorded employing a FLUOstar OPTIMA (BMG Labtech, Ortenburg, Germany).

### 2.17 | Data analysis and statistics

Data analysis and illustrations were performed using Microsoft Excel, GraphPad Prism, ImageJ and BioRender. Two-tailed paired or unpaired Student's t-test was used to compare AA and ctrl. within a cell line. When comparing both AA and ctrl. in multiple treatments, two-way analysis of variance (ANOVA) with Tukey's or Bonferroni's multiple comparison post-test was used. Unless otherwise stated, bars show mean, points individual experiments, and error bars SE of the Mean (SEM). In graphs of normalized data from more than 2 cell lines, each AA cell line is compared with its normalized ctr. shown as a dotted line.

## 3 | RESULTS

### 3.1 | Cancer cells growing in chronic acidosis upregulate net acid extrusion

To study mechanisms of cancer cell adaptation in acidic TME regions in vitro, we adapted multiple human cancer cell lines (Panc1, MDA-

MB-231, MCF-7 and HCT116) to growth at pH<sub>e</sub> 7.6 and 6.5, by adjusting [HCO<sub>3</sub><sup>-</sup>] in the medium and maintaining cells at 5% CO<sub>2</sub>, followed by a series of experiments to unravel cellular genotype and phenotype (Figure 1A). Cell lines will be referred to as for example, *Panc-1-ctrl.* and *Panc-1-AA*, where “ctrl.” refers to cells growing at pH<sub>e</sub> 7.6 and “AA” refers to cells adapted to growth at pH<sub>e</sub> 6.5. It should be noted that tumors display a wide range of pH values in the acidic range, from ~5.6 to around 7.0 (see<sup>2</sup>). A pH of 6.5 is thus well within the range of values found in the literature.

Acute intracellular acidification limits proliferation and growth of normal cells.<sup>12</sup> In striking contrast, acid-adapted cancer cells were not, or only marginally (MDA-MB-231 cells) growth-limited at pH<sub>e</sub> 6.5, as assessed by BrdU incorporation (Figure 1B) and Retinoblastoma protein (pRb) hyperphosphorylation (Figure 1C,D).

As shown across multiple cancer cell lines,<sup>22</sup> acidification of pH<sub>e</sub> causes a corresponding albeit less pronounced acidification of pH<sub>i</sub>, driven by the increased inward driving force for H<sup>+</sup>. However, the vast majority of measurements of cancer cell pH<sub>i</sub> are performed in a pH 7.4 medium, where the inward-driving force for H<sup>+</sup> is several-fold smaller than at the pH 6.5 in acidic tumor regions, leading to a more alkaline pH<sub>i</sub>. We therefore asked what the steady state pH<sub>i</sub> was in cancer cells adapted and growing at pH<sub>e</sub> 6.5, using the most aggressive cell lines studied, Panc-1 and MDA-MB-231 cells. pH<sub>i</sub> was determined by real time imaging in Ringer solutions set to the desired pH at 5% CO<sub>2</sub> by adjusting [HCO<sub>3</sub><sup>-</sup>]. Under these conditions, pH<sub>i</sub> in acid-adapted cells was ~pH 6.8 in both cell types, compared with ~7.3 in control cells at pH 7.4 (Figure 1E). We next asked how this would change when cancer cells from an acidic niche encounter normal tissue pH<sub>e</sub>, for example, during invasion or an increase in local perfusion. Strikingly, when measured at pH<sub>e</sub> 7.4, to simulate such a scenario, pH<sub>i</sub> was much more alkaline in AA cells than in ctrl. cells, reaching up to pH<sub>i</sub> 7.6 (Figure 1F). This has two possible, not mutually exclusive, interpretations: net acid extrusion could be upregulated, and/or net acid production downregulated, in AA cells compared with controls.

To gain insight into this, we first performed immunoblotting for the Na<sup>+</sup>/H<sup>+</sup> exchanger NHE1, the Na<sup>+</sup>-HCO<sub>3</sub><sup>-</sup> cotransporter NBCn1, and the H<sup>+</sup> V-ATPase, key net acid-extruding transporters in cancer cells.<sup>2</sup> The NHE1 protein level was only increased in a subset of cell lines and decreased in others (Figures 1G and S1A). Strikingly however, the NBCn1 protein level was increased in all AA cells compared

**FIGURE 1** Acid-adapted cancer cells exhibit acidic steady state pH<sub>i</sub> at acidic pH<sub>e</sub>, yet elevated pH<sub>i</sub> at normal pH<sub>e</sub>. (A) Experimental strategy. WT Panc-1, MDA-MB-231 (MDA), MCF-7 and HCT116 (HCT) cells were adapted to pH<sub>e</sub> 7.6 or 6.5 over a period of minimum 4 weeks. (B) Cell proliferation assessed by BrdU analysis (n = 9, 11, 7, 6 for Panc-1, MDA, MCF-7 and HCT, respectively). (C, D) Representative Western blot (C) and quantification (D) of pSer807/811-pRb. Dynactin subunit 1 (DCTN1) was used as loading control (n = 5, 8, 5, 3 for Panc-1, MDA, MCF-7 and HCT, respectively). (E, F) BCECF-AM fluorescence converted to steady state pH<sub>i</sub> at pH<sub>e</sub> 7.6 or 6.5 (E) and pH<sub>e</sub> 7.4 (F). Points indicate individual measurements. Horizontal line denotes median, and upper and lower lines indicate max. and min. values, respectively (n = 7, 11 (Panc-1 ctrl., AA); 6, 8 (MDA ctrl., AA) for panel E; and n = 8, 7 (Panc-1 ctrl., AA); 7, 6 (MDA ctrl., AA), 4, 6 (MCF-7 ctrl., AA); 4, 5 (HCT ctrl., AA) for panel F). (G-J) Representative Western blots (G, H, I) and quantifications (I) of NHE1 (G), NBCn1 (H) and V-ATPase (B2 subunit) (I). Histone H3 (H3) or DCTN1 was used as loading controls as indicated (n = 6, 4 for Panc-1 and MDA, respectively, for panel I). For (B, D, E, F, I), dotted line indicates ctrl. value and an unpaired two-tailed t-test was performed for each individual cell line, AA vs ctrl. (p values indicated on top). (J) Representative IF images and zooms (white boxes) of V-ATPase (B2 subunit) (green), F-actin (magenta) and DAPI (blue). Arrowheads denote membrane localization of V-ATPase (B2 subunit). Image overlays and adjustments of the intensities were performed using ImageJ software. Scale bars: 20 µm. n = 3

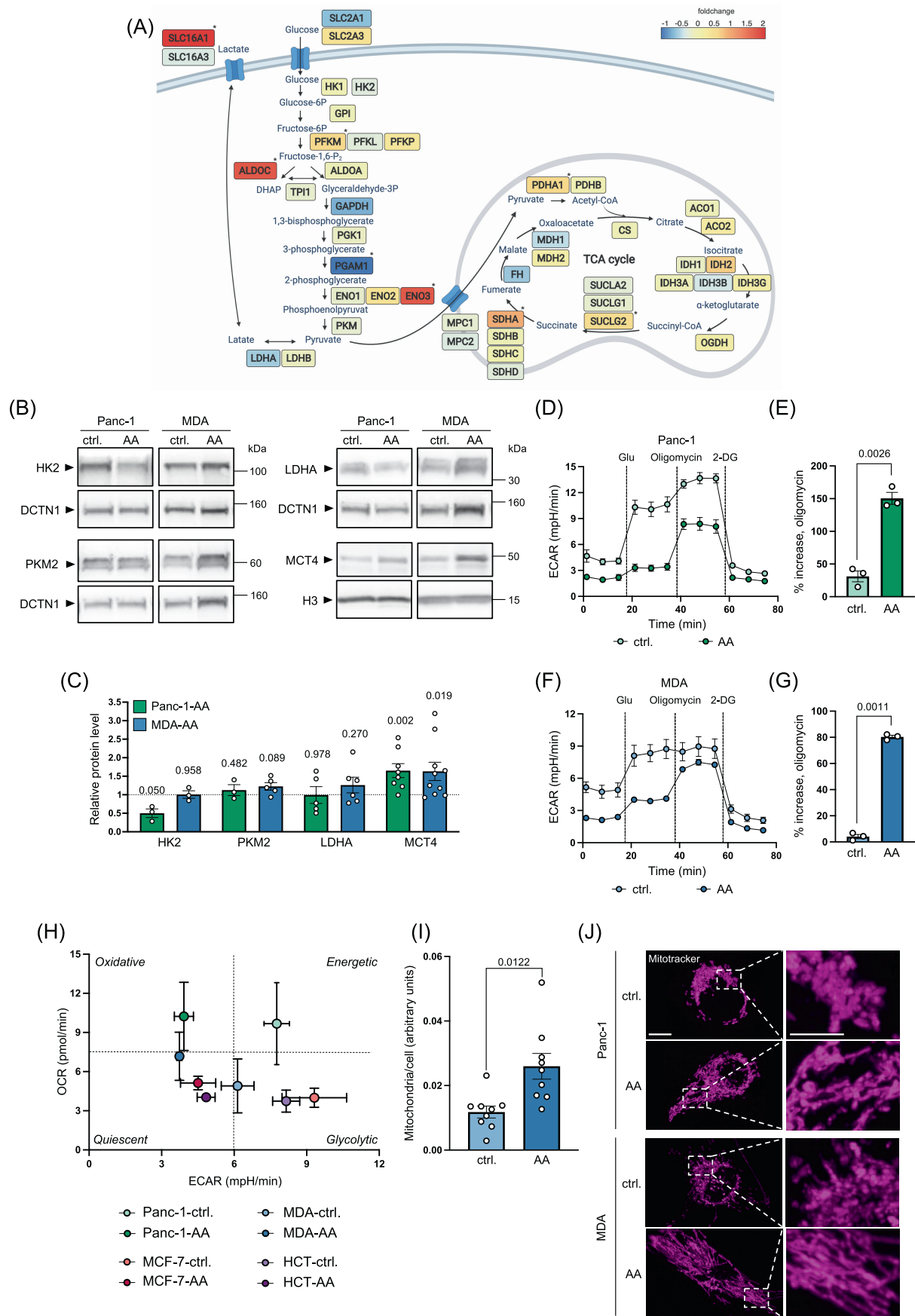


FIGURE 2 Legend on next page.

with ctrl. cells (Figures 1H and S1B). In MDA-MB-231-AA cells we additionally observed an increase in protein level and plasma membrane localization of the ubiquitous V-ATPase subunit B2, indicating that V-ATPase-mediated H<sup>+</sup> extrusion may contribute to acid extrusion in these cells (Figure 1I, J, white arrowheads in J).

These results show that cancer cells growing in acidic environments upregulate net acid extruders. Under the large inward-directed H<sup>+</sup> driving force at pH<sub>e</sub> 6.5, this is not sufficient to normalize pH<sub>i</sub>, which remains modestly acidic. At pH<sub>e</sub> 7.4, pH<sub>i</sub> of acid-adapted cells becomes alkaline, a condition expected to endow them with a growth advantage.

### 3.2 | Acid adaptation reduces glucose-dependent acid extrusion but maintains glycolytic capacity

We next asked whether cancer cells cultured under acidic conditions also altered their metabolic activity to produce less acid. We recently reported RNA-seq analysis of differentially expressed (DE) genes in several ctrl.- and AA cell types.<sup>25</sup> To delineate the metabolic changes occurring in AA cells using these data, we focused on the two most aggressive cell lines, Panc-1 and MDA-MB-231 (Tables S3-S4). KEGG pathway analysis showed shifts in expression of glycolytic- as well as TCA cycle- and OXPHOS genes (FDR < 0.05) in MDA-MB-231-AA cells compared with control cells, with no obvious shift from one pathway to the other (Figure 2A and S2A). Similar changes were seen in Panc-1-AA cells (Figure S2B and S3A,B). The pattern was

confirmed at the protein level for the key glycolytic enzymes Hexokinase 2 (HK2) (Figure 2B, C), pyruvate kinase isozyme M2 (PKM2) (Figure 2B, C), lactate dehydrogenase (LDHA) (Figure 2B, C), and the monocarboxylate transporter SLC16A3 (MCT4) (Figure 2B, C). While not further addressed here, a full gene set enrichment analysis additionally revealed major upregulation of genes related to extracellular matrix organization in both MDA-MB-231-AA and Panc-1-AA cells, and downregulation of genes related to DNA replication and cell cycle specifically in Panc-1-AA cells, compared with controls (Figure S4).

To gain functional insight into the metabolic phenotype imposed by acid adaptation, we performed a glycolytic stress test in MDA-MB-231, Panc-1 (Figure 2D, F), MCF-7 and HCT116 cells (Figure S5A, C). All cell lines showed a consistent pattern of changes upon acid adaptation: compared with ctrl. cells, AA cells exhibited a reduced non-glycolytic extracellular acidification rate (ECAR, Figures 2D, F and S5A, C) prior to glucose addition—usually interpreted as deriving from glycolysis-independent TCA-cycle-derived CO<sub>2</sub><sup>31</sup>—and glucose-induced ECAR was reduced in all AA cell lines compared with ctrl. (Figures 2D, F and S5A, C). Strikingly, the increase in ECAR upon ATP synthase inhibition by oligomycin—representing maximal glycolytic capacity—was strongly increased in all AA cell lines compared with controls (Figures 2D-G and S5A-D). Mirroring this, oligomycin addition elicited a correspondingly greater decrease in oxygen consumption rate (OCR) in AA cells (Figure S5E-H). Thus, AA cells exhibit a shift toward oxidative metabolism, but, importantly, retain substantial glycolytic capacity, and can rapidly switch when oxidative metabolism

**FIGURE 2** Acid-adapted cells exhibit reduced glucose-dependent acid extrusion but maintain glycolytic capacity. (A) Overview of the expression level of genes involved in glycolysis and TCA-cycle in MDA-AA cells compared with MDA-ctrl. Color indicates average log2 fold change across three replicates per condition. The asterisk indicates statistical significance ( $P < .05$ , AA vs ctrl.). (B, C) Representative Western blots (B) and quantifications (C) of HK2, PKM2, LDHA and MCT4. DCTN1 or H3 was used as loading control as indicated. For PKM2 and LDHA, the same loading ctrl is used, as these two proteins were derived from the same blot. In (C) the dotted line indicates ctrl. value. A paired (MCT4) or unpaired (HK2, PKM2 and LDHA) two-tailed t-test was performed for each individual cell line, AA vs ctrl. ( $p$  values indicated on top;  $n = 3$ , 3 (HK2); 3, 5 (PKM2); 5, 6 (LDHA); 8, 11 (MCT4) for Panc-1 and MDA, respectively). (D, F) Extracellular acidification rate (ECAR, mpH/min) as a function of time in Panc-1 (D) and MDA (F). At the indicated time points, glucose (Glu, 10  $\mu$ M), oligomycin (1  $\mu$ M) and 2-deoxy-glucose (2-DG, 50 mM) was added to each well followed by three sets of three measurements over a time period of  $\sim$ 18 min. In each biological replicate, at least 15 technical replicates were measured.  $n = 3$ . (E, G) Calculated percent increase in ECAR between glucose (average of data points 4-6) and oligomycin (average of data points 7-9) conditions in Panc-1 (E) and MDA (G). A paired two-tailed t-test was performed for each individual cell line, AA vs ctrl. ( $p$  values are indicated on top;  $n = 3$ ). (H) Average oxygen consumption rate (OCR, pmol/min) as a function of average ECAR (mpH/min) of Panc-1, MDA, MCF-7 and HCT ctrl. and AA cells. Error bars represent S.E.M values.  $n = 3$  for Panc-1 and MDA and 4 for MCF-7 and HCT. (I) Mitochondrial content in MDA-AA compared with MDA-ctrl. cells. Mitochondria were quantified by MitoTracker Green and normalized to cell number in each experiment using Hoechst staining. In each experiment, three technical replicates were performed. A paired two-tailed t-test was performed for each individual cell line, AA vs ctrl. ( $p$  value is indicated on top;  $n = 8$ ). (J) Representative IF images of mitochondria visualized with MitoTracker Deep Red (magenta) in Panc-1 and MDA ( $n = 3$ ). Image overlays and adjustments of the intensities were performed using ImageJ software. Scale bar: 10 and 5  $\mu$ m for full and zoomed image, respectively. Abbreviations for Figure 2: ACO1/2, aconitase 1/2; ALDOA/C, fructose-biphosphate aldolase A/C; CS, citrate synthase; ENO1/2/3, enolase 1/2/3; GAPDH, glyceraldehyde-3-phosphate dehydrogenase; GPI, glucose-6-phosphate isomerase; HK1/2, hexokinase 1/2; IDH1/2, isocitrate dehydrogenase 1/2; IDH3A, isocitrate dehydrogenase 3 catalytic subunit alpha; IDH3B, isocitrate dehydrogenase 3 non-catalytic subunit beta; IDH3G, isocitrate dehydrogenase 3 non-catalytic subunit gamma; LDHA/B, lactate dehydrogenase A/B; MP1/2, mitochondrial pyruvate carrier 1/2; OGDH, oxoglutarate dehydrogenase; PDHA1/B, pyruvate dehydrogenase E1 subunit alpha 1/beta; PFKL/M/P, phosphofructokinase, liver/muscle/platelet; PGAM1, phosphoglycerate mutase 1; PGK1, phosphoglycerate kinase 1; PKM, pyruvate kinase M1/M2; SDHA, succinate dehydrogenase complex flavoprotein subunit A; SDHB, succinate dehydrogenase complex iron sulfur subunit B; SDHC/D, succinate dehydrogenase complex subunit C/D; SLC16A1/3, solute carrier family 16 member 1/3; SLC2A1/3, solute carrier family 2 member 1/3; SUCLA2, succinate-CoA ligase ADP-forming subunit beta; SUCLG1, succinate-CoA ligase GDP/ADP-forming subunit alpha; SUCLG2, succinate-CoA ligase GDP-forming subunit beta; TPI1, triosephosphate isomerase 1



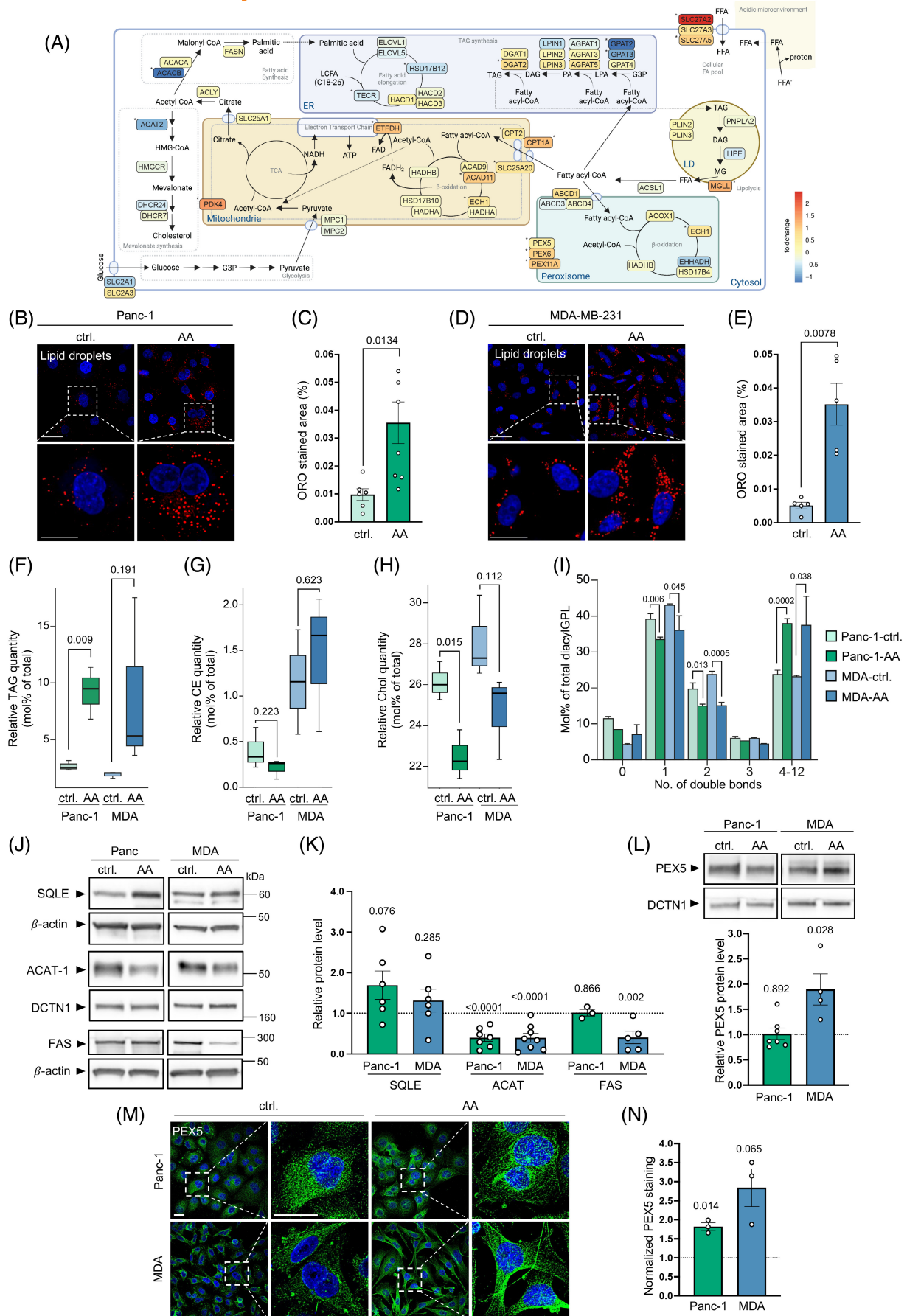


**FIGURE 3** Legend on next page.

is inhibited. ECAR and OCR data for all cell lines are summarized in Figure 2H, confirming that control cells are predominantly glycolytic, and AA cells predominantly oxidative. This was further corroborated by the finding that microenvironment acidosis was associated with increased mitochondrial mass per cell, as quantified from total mitotracker fluorescence normalized to cell number (Figures 2I and S5I), and with elongated mitochondrial morphology as assessed by high resolution Airy scan imaging of mitotracker fluorescence (Figure 2J). These changes in mitochondrial morphology were confirmed by IF analysis of mitochondrial outer membrane protein TOM20 (Figure S5J). Increased mitochondrial mass and elongated branches generally correspond to increased oxidative phosphorylation capacity,<sup>32</sup> and together with the altered expression of mitochondrial genes, this morphological change is therefore likely an adaptive response to the acidic microenvironment.

Collectively, these data show that AA cells exhibit increased mitochondrial mass, apparent branch elongation, and an oxidative shift in presence of glucose and oxygen. Importantly however, the cells retain a large glycolytic capacity, suggesting that they exhibit increased metabolic plasticity.

### 3.3 | Acid adaptation is associated with increased lipid accumulation and peroxisomal mass

Our RNA-seq analyses showed that genes associated with fatty acid (FA) degradation were significantly upregulated in AA cells. Pathway

maps of these data are shown in Figure 3A for MDA-MB-231 cells, and in Figure S6 for Panc-1 cells. Altered FA metabolism, including increased lipid droplet (LD) content, is a characteristic of many cancers.<sup>33</sup> CD36-mediated uptake of FAs in AA cells followed by storage in LDs was recently reported, with accumulation in LDs suggested to protect cells against lipotoxicity.<sup>9</sup> In congruence with this, LD content, evaluated by Oil-Red-O staining, was markedly elevated in AA— compared with ctrl. cells (Figure 3B-E). To further understand the changes in FA metabolism imposed by acidic growth, we used shotgun lipidomics to study the acid adaptation-induced changes in cellular lipid composition. Consistent with the high triacylglyceride (TAG) content of LDs,<sup>33</sup> total TAG content was strongly increased in AA- compared with ctrl. cells (Figure 3F). Total content of the other major LD constituent, cholesterol esters (CE), was not consistently altered, and total cholesterol was modestly reduced, in both Panc-1-AA and MDA-MB-231-AA cells (Figure 3G-H).

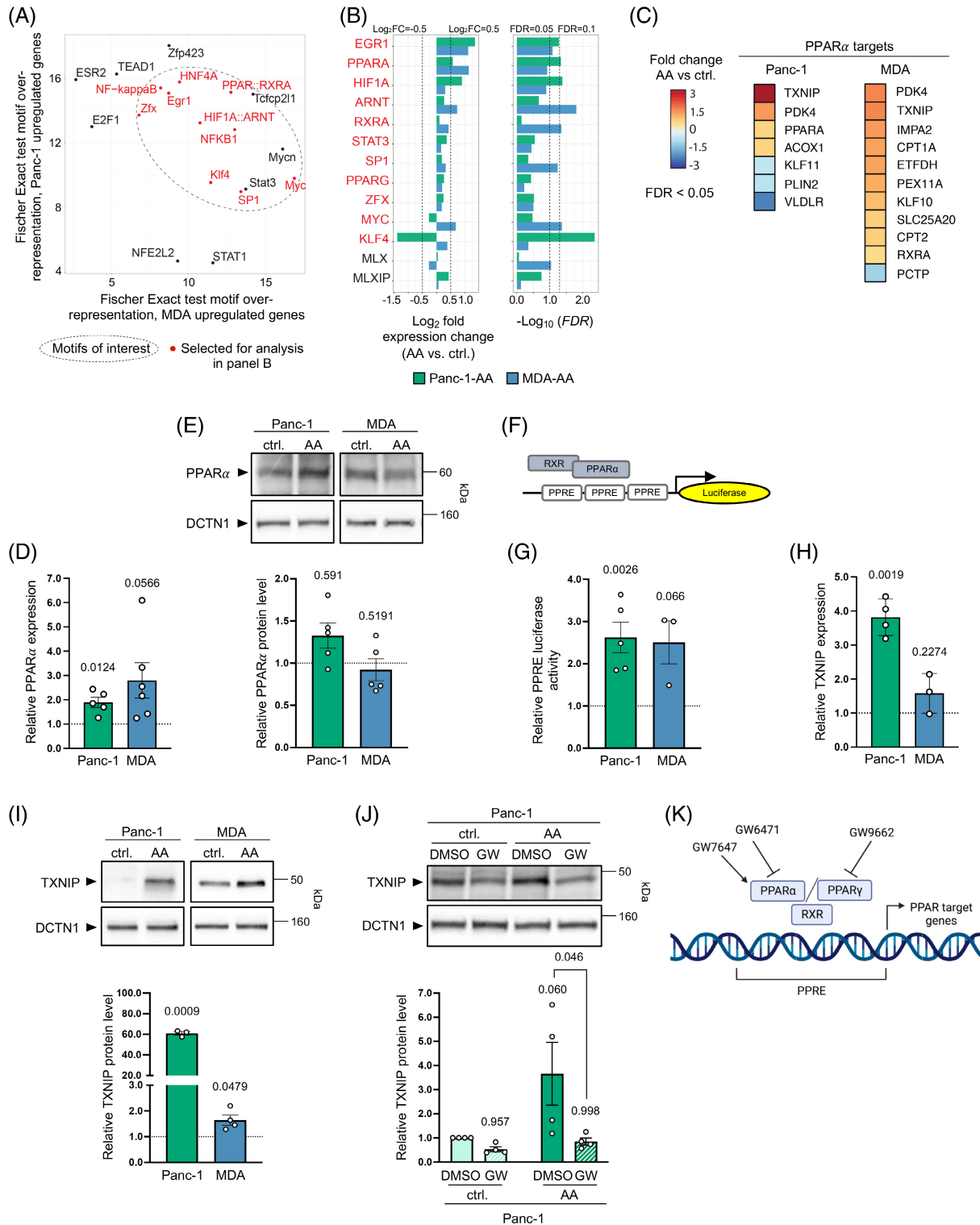
To gain insight into the origin of the FAs accumulating in AA cells, we studied the diacylglycerophospholipid (diacylglycerophospholipid) composition using shotgun lipidomics. Interestingly, acidic growth was associated with a significant increase in diacylglycerophospholipids with multiple (4-12) double bonds and a corresponding decrease in diacylglycerophospholipids with only 1-2 double bonds (Figure 3I). In particular, a large fraction of diacylglycerophospholipids in AA cells had ≥4 double bonds in the two FA chains together, suggesting that the bulk of these diacylglycerophospholipids has incorporated essential polyunsaturated FAs from the growth medium serum. In agreement with the notion that the increased TAG levels in AA cells reflect uptake rather than FA production, expression of fatty acid synthase (FAS) was

**FIGURE 3** Acid adaptation causes major changes in cellular lipid composition. (A) Overview of the expression level of genes involved in fatty acid metabolism in MDA-AA cells compared with MDA-ctrl. Color indicates average log2 fold change across three replicates per condition. The asterisk indicates statistical significance (FDR < .05, AA vs ctrl.). Major pathways are denoted in light gray. Specific organelles are shown as colored boxes. Cytosolic pathways are separated by boxes with dotted lines. (B-E) Representative images and zooms (white boxes) of Oil-red-O-stained lipid droplets (B, D) and quantification (C, E) in Panc-1 and MDA, respectively. An unpaired (C) or paired (D) two-sided *t*-test was performed for each individual cell line, AA vs ctrl. (*p* values are given on top; *n* = 6, 4 for Panc-1 and MDA, respectively). Scale bars: 40 and 20 μm for full and zoomed images, respectively. (F-H) Relative molar quantity (mol%) of triacylglycerides (TAG), (F) cholesterol (Chol), (G) and cholesteryl esters (CE) (H) measured by shotgun lipidomics. Horizontal line denotes median, and upper and lower lines indicate max. and min. values, respectively. (I) Relative molar quantity of diacylglycerophospholipids (diacylglycerophospholipids) with the indicated number of acyl double bonds in Panc-1 and MDA. For (F-I) A multiple unpaired two-sided *t*-test was performed, AA vs ctrl. (*p* values shown on top; *n* = 3). (J, K) Representative Western blots (J) and quantifications (K) of SQLE, ACAT-1 and FAS. β-actin (SQLE, FAS) or DCTN1 (ACAT-1) was used as loading control. An unpaired two-sided *t*-test was performed for the individual cell lines, AA vs ctrl. (*p* values are given on top; *n* = 6 (SQLE); 7, 8 (ACAT-1); 3, 5 (FAS) for Panc-1 and MDA, respectively. (L) Representative Western blots and quantification of PEX5. DCTN1 was used as loading control. An unpaired two-sided *t*-test was performed for the individual cell lines, AA vs ctrl. (*p* values are given on top; *n* = 7, 4 for Panc-1 and MDA, respectively. (M, N) Representative IF images and zooms (white boxes) of PEX5 (M) and quantification (N). Scale bar: 20 μm. A paired two-sided *t*-test was performed for the individual cell lines, AA vs ctrl. (*p* values are given on top; *n* = 3). For (K, L, N) dotted line indicates ctrl. value. Abbreviations for Figure 3: ABCD1/3/4, ATP binding cassette subfamily D 1/3/4; ACACA/B, acetyl-CoA carboxylase alpha/beta; ACAD9/11, acyl-Coa dehydrogenase 9/11; ACAT2, acetyl-CoA acetyltransferase 2; ACLY, ATP citrate lyase; ACOX1, acyl-CoA oxidase 1; ACSL1, acetyl-CoA synthetase long chain 1; AGPAT1/3/5, 1-acylglycerol-3-phosphate O-acyltransferase 1/3/5; CPT1A/2, carnitine palmitoyltransferase 1A/2; DGAT1/2, diacylglycerol O-acyltransferase 1/2; DHCR7/24,7/24-dehydrocholesterol reductase; ECH1, enoyl-CoA hydratase 1; EHHADH, enoyl-CoA hydratase and 3-hydroxyacyl CoA dehydrogenase; ELOVL1/5, ELOVL fatty acid elongase 1/5; ETFDH, electron transfer flavoprotein dehydrogenase; FASN, fatty acid synthase; GPAT2/3/4, glycerol-3-phosphate acyltransferase 2/3/4; HACD1/2/3, 3-hydroxyacyl-CoA dehydrogenase 1/2/3; HADHA/B, hydroxyacyl-CoA dehydrogenase trifunctional multienzyme complex subunit alpha/beta; HMGCR: 3-hydroxy-3-methylglutaryl-CoA reductase; HSD17B4/10/12, hydroxysteroid 17-beta dehydrogenase 4/10/12; LIPE, lipase E; LPIN1/2/3, Lipin 1/2/3; MGLL, monoglyceride lipase; MPC1/2, mitochondrial pyruvate carrier 1/2; PDK4, pyruvate dehydrogenase kinase 4; PEX5/6/11A, peroxisomal biogenesis factor 5/6/11 alpha; PLIN2/3, Perilipin 2/3; PNPLA2, patatin like phospholipase domain containing 2; SLC25A1/20, solute carrier family 25 member 1/20; SLC27A1/3/5, solute carrier family 27 member 1/3/5; SLC2A1/3, solute carrier family 2 member 1/3; TECCR, trans-2,3-enoyl-CoA reductase

unaltered in Panc-1-AA and strongly reduced in MDA-MB-231-AA cells (Figure 3J-K), and expression of genes involved in FA elongation was not increased (Figures 3A and S6 and Tables S3 and S4). Consistent with the lack of changes in cholesterol and cholesterol ester levels in AA cells, protein levels of squalene epoxidase (SQLE), and acyl-coenzyme-A: cholesterol acyltransferase (ACAT), key enzymes in

cholesterol- and cholesterol ester biosynthesis were not increased in AA cells (Figure 3J-K).

Genes upregulated in AA cells included the carnitine palmitoyl-transferases CPT1A and CPT2, as well as SLC25A20, the gene encoding carnitine-acylcarnitine translocase (CACT)—collectively the components of the carnitine cycle required for transport of long-chain



FAs to the intramitochondrial space for  $\beta$ -oxidation (Figures 3A and S6). These changes support increased FA uptake into mitochondria. However, not only mitochondria but also peroxisomes are important sites of fatty acid  $\beta$ -oxidation, and peroxisomes play a particularly important role in oxidation of very long chain FAs (VLCFAs).<sup>34</sup> Accordingly, a striking number of peroxisomal genes were upregulated in AA cells, including Peroxisomal biogenesis factor 5 (PEX5), PEX11A, other PEX isoforms, and acyl-coenzyme A oxidase 1 (ACOX1), the main enzyme responsible for peroxisomal oxidation of VLCFAs<sup>34</sup> (Figures 3A and S6 and Tables S1 and S2). PEX5 upregulation was confirmed at the protein level in MDA-MB-231-AA cells (Figure 3L), and cellular peroxisome content, determined by quantitative IF analysis of PEX5, was increased  $\sim$ 1.7-fold in Panc-1-AA cells and  $\sim$  3-fold in MDA-MB-231-AA cells (Figure 3M-N).

Collectively, these data indicate that cancer cells growing in an acidic environment increase FA uptake and upregulate mitochondrial and peroxisomal lipid uptake- and  $\beta$ -oxidation capacity.

### 3.4 | Increased PPAR $\alpha$ signaling in AA cells leads to upregulation of TXNIP and other PPAR $\alpha$ targets

We next asked which pathways could underlie the acid-driven changes in lipid metabolism, mitochondrial lipid uptake and peroxisomal biogenesis. Analysis of transcription factor binding site using oPOSSUM<sup>29</sup> showed that the peroxisome proliferator response element (PPRE) was one of the most over-represented sequence patterns in promoters of genes upregulated in Panc-1-AA and MDA-MB-231-AA compared with ctrl. cells (Figure 4A). PPREs are bound by

peroxisome proliferator-activated receptors (PPARs,  $\alpha$ ,  $\beta/\delta$  and  $\gamma$ ), acting as heterodimers with nuclear Retinoid X receptor alpha (RXRA).<sup>35</sup> PPAR $\alpha$ , but neither PPAR $\beta/\delta$  nor PPAR $\gamma$ , was upregulated in AA cells (Figure 4B and Tables S1 and S2). PPAR $\alpha$  is a pivotal regulator of lipid metabolism and stimulated by polyunsaturated FAs,<sup>35</sup> and we therefore pursued this further. KEGG analysis showed that a striking number of upregulated genes were well-established PPAR $\alpha$  targets, including PEX11A, CPT1A, CPT2, SLC25A20, ACOX1, Electron Transfer Flavoprotein Dehydrogenase (ETFHDH, essential part of the electron transport chain), PDK4, which has been shown to contribute to PPAR $\alpha$ -induced fatty acid oxidation,<sup>36</sup> and finally, the master metabolic regulator thioredoxin-interacting protein (TXNIP) (Figure 4C).<sup>35</sup> Notably, the transcription factor MondoA (MLXIP) and its binding partner MLX, which can also drive TXNIP expression<sup>24</sup> were not highly expressed, and their expression was unaltered by acid adaptation (Figure 4A,B and Tables S1 and S2).

qPCR analysis (Figure 4D) confirmed the PPAR $\alpha$  upregulation, while PPAR $\alpha$  protein levels (Figure 4E) were not consistently upregulated in AA cells. Importantly, PPAR transcriptional activity assessed as PPRE-driven luciferase expression was strongly increased in both Panc-1-AA and MDA-MB-231-AA cells, consistent with the upregulation of PPAR $\alpha$  targets (Figure 4F-G). Upregulation of PPRE-mediated transcriptional activity by the PPAR $\alpha$ -specific agonist GW7647 (Figure S7A) and downregulation by PPAR $\alpha$  antagonist GW6471 (Figure S7B) validated assay sensitivity to PPAR $\alpha$  activity. To confirm that target regulation was driven by PPAR $\alpha$ , we studied TXNIP. Consistent with the RNA-seq data, mRNA and protein levels of TXNIP were upregulated in both Panc1-AA and MDA-MB-231-AA cells (Figure 4H-I). This upregulation was abolished by the PPAR $\alpha$ -specific antagonist

**FIGURE 4** PPAR $\alpha$ -driven gene expression is upregulated in acid-adapted cells. (A) Transcription factor binding site over-representation analysis. The x- and y-axis show the Fisher exact test over-representation statistic for the top 15 over-represented JASPAR motifs in the  $\pm$ 5 kbp region around the start sites of upregulated genes (AA vs ctrl., FDR < 0.05), using the Opossum tool. Each dot represents one motif; JASPAR motif names are shown. Motifs inside the dotted circle were used for follow up-expression analyses in (B), but only linked genes with detected expression levels were considered (with the exception of PPAR $\alpha$ : see below). Motif names with “::” correspond to transcription factor heterodimers. (B) Expression change of chosen transcription factor genes. Panels show  $\log_2$  fold change and associated FDR values (AA vs ctrl.) based on RNA-sequencing data. Each row corresponds to one gene; red genes were selected based on (A). In case of dimers, both genes were investigated. PPAR $\alpha$  was included since PPAR $\alpha$  showed no expression change and the two proteins have similar binding preferences. The MLXIP and MLX genes (black) are described in the main text. Rows are sorted by average  $\log_2$  fold. (C) Heatmap visualization of significantly DE PPAR $\alpha$  targets (AA vs ctrl., FDR < 0.05). Color indicates average  $\log_2$  fold change of DE genes (AA vs ctrl.) across three replicates per condition. (D) Relative mRNA levels (qPCR) of PPAR $\alpha$ . Data is normalized to an average of  $\beta$ -actin and TATA-binding protein (TBP). A paired two-sided *t*-test was performed for each individual cell line, AA vs ctrl. (*p* values shown on top of bars; *n* = 5, 6 for Panc-1 and MDA, respectively). (E) Representative Western blots and quantification of PPAR $\alpha$ . DCTN1 was used as loading control. An unpaired two-sided *t*-test was performed for each individual cell line, AA vs ctrl. (*p* values shown on top of bars; *n* = 5). (F) Schematic of the PPRE-X3-Luc plasmid. (G) Relative PPAR $\alpha$ -mediated Firefly luciferase signal normalized to pRL-TK-mediated Renilla luciferase signal measured by the dual-luciferase assay. Data was log-transformed prior to comparison to improve normal distribution. A paired two-sided *t*-test was performed on the log-transformed values for each individual cell line, AA vs ctrl. (*p* values shown on top of bars; *n* = 5, 3 for Panc-1 and MDA, respectively). (H) Relative mRNA levels (qPCR) of TXNIP. Data is normalized to an average of  $\beta$ -actin and TBP. An unpaired two-sided *t*-test was performed for each individual cell line, AA vs ctrl. (*p* values shown on top of bars; *n* = 4, 3 for Panc-1 and MDA, respectively). (I) Representative Western blots and quantification of TXNIP. DCTN1 was used as loading control. A paired two-sided *t*-test was performed for each individual cell line, AA vs ctrl. (*p* values shown on top of bars; *n* = 3, 4 for Panc-1 and MDA, respectively). (J) Panc-1 cells were treated with GW6471 (GW, PPAR $\alpha$  antagonist, 1  $\mu$ M) or vehicle control (DMSO) for 24 h. Representative Western blots and quantifications of TXNIP. DCTN1 was used as loading control. Two-way ANOVA with Tukey's post-test (*n* = 4). When compared with DMSO for ctrl. cells, *p* values are directly above the bar. Comparison of two treatments is indicated by connecting lines with *p* values given on top. For (D, E, G, H, I, J) dotted line indicates ctrl. value. (K) Illustration of the targets of the used agonist and antagonists

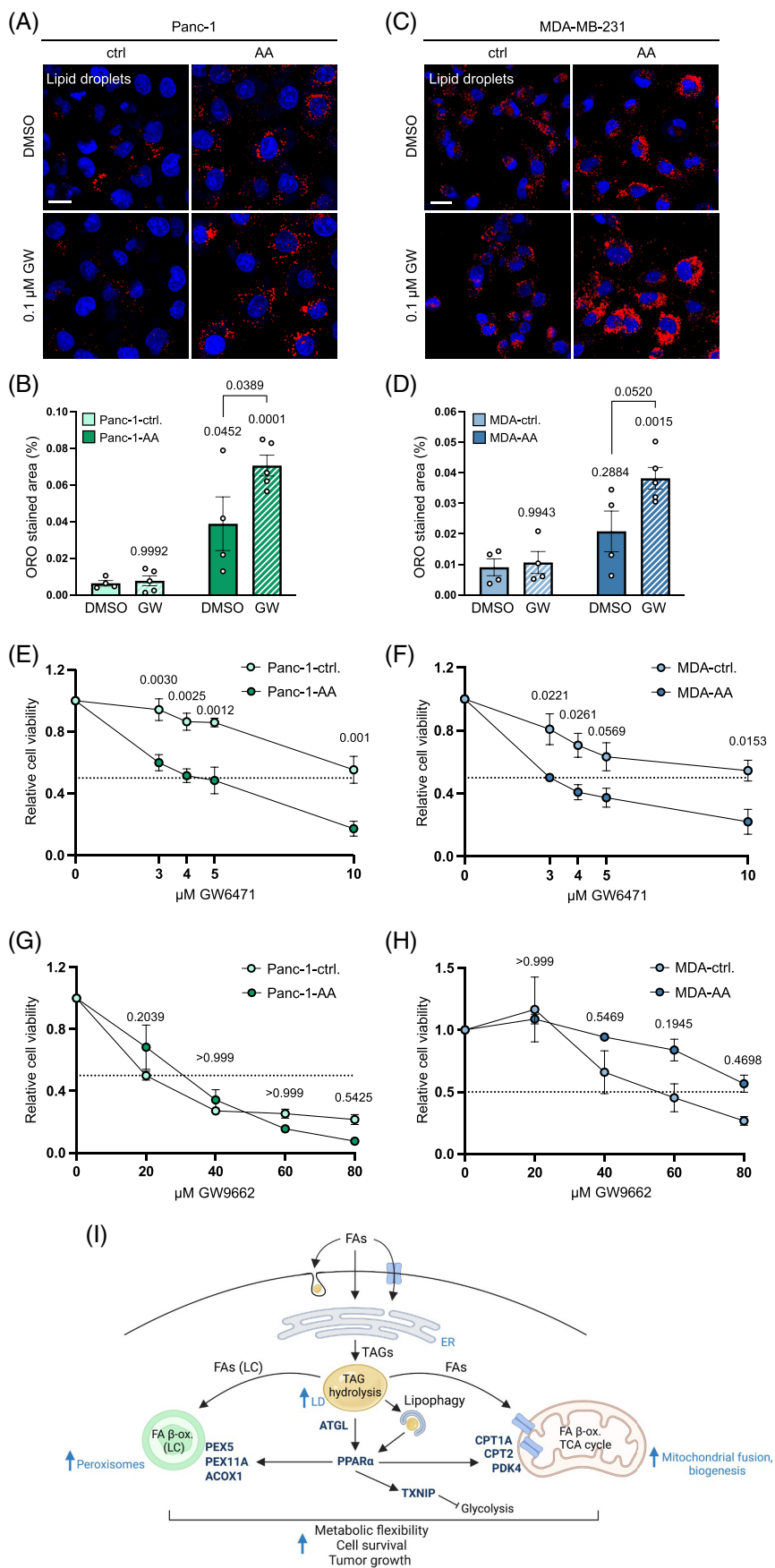


**FIGURE 5** Acid-adapted cells exhibit increased sensitivity to PPAR $\alpha$  inhibition. (A–D) Panc-1 and MDA cells grown on coverslips were treated with GW6471 (GW, PPAR $\alpha$  antagonist, 0.1  $\mu$ M) or DMSO for 24 h and stained for lipid droplets with Oil-red-O. Representative images of Oil-red-O-stained lipid droplets (A, C) and quantification (B, D) for Panc-1 and MDA, respectively. Scale bar: 20  $\mu$ m. Two-way ANOVA with Tukey's post-test ( $n = 4$ –5). When compared with DMSO for ctrl. cells,  $p$  values are directly above the bar. Comparison of two treatments is indicated by connecting lines with  $p$  values given on top. (E–H) Panc-1 and MDA cells were treated with increasing doses of either GW6471 (PPAR $\alpha$  antagonist, E, F) or GW9662 (PPAR $\gamma$  antagonist, G, H) or DMSO for 72 h. Graphs display cell viability assessed by CellTiter Glo normalized to the respective DMSO. The dotted line indicates 50% cell death. A paired two-way ANOVA with Bonferroni's post-test was used to test for statistical differences between ctrl. and AA at each concentration;  $p$  values are directly above the corresponding concentration ( $n = 3$  for MDA and 5 to 6 for Panc-1 for F and G, respectively). (I) Working hypothesis: Upon acid adaptation, increased fatty acid uptake and TAG hydrolysis drive upregulation of PPAR $\alpha$  and its target genes including TXNIP and peroxisomal and mitochondrial genes. This enables increased  $\beta$ -oxidation and metabolic flexibility, facilitating cancer cell survival and growth in the acidic TME. LC, long chain. See text for details

GW6471 (Figure 4J), confirming that it was specifically driven by PPAR $\alpha$ . Figure 4K summarizes the PPAR inhibitors used in Figures 4, 5 and S7.

These results show that PPAR $\alpha$  is upregulated in acid-adapted cancer cells, resulting in upregulation of multiple PPAR $\alpha$  targets.

### 3.5 | Cancer cells in the acidic tumor microenvironment exhibit increased sensitivity to PPAR $\alpha$ inhibition

We reasoned that if cells growing in acidic conditions exhibit increased FA uptake followed by their utilization through mitochondrial and peroxisomal lipid  $\beta$ -oxidation, and if PPAR $\alpha$  is more important for degradation than for uptake of the FAs,<sup>37</sup> PPAR $\alpha$  inhibition should increase lipid accumulation. To test this, we assessed the effect of GW6471 on LD content in control and AA cells (Figure 5A-D). Treatment with the antagonist increased LD content in both Panc1-AA and MDA-MB-231-AA cells, while having no effect in control cells, indicating that indeed, FA utilization was more reliant on PPAR $\alpha$  than was FA import.

If AA cells exhibit increased dependence on PPAR $\alpha$ -driven FA degradation for growth and survival, they should be more sensitive than control cells to PPAR $\alpha$  inhibition. To test this, we determined cell viability upon treatment with increasing concentrations of GW6471. To evaluate specificity for PPAR $\alpha$ , we also treated cells with the PPAR $\gamma$  antagonist GW9662. Strikingly, both Panc-1-AA and MDA-MB-231-AA cells exhibited greatly increased sensitivity to PPAR $\alpha$  inhibition compared with control cells (Figure 5 E-F). The opposite was true for PPAR $\gamma$  inhibition, which was equally (Panc-1) or more (MDA-MB-231) detrimental to growth of control cells (Figure 5G-H).

These data show that cancer cells in an acidic microenvironment exhibit increased dependence on PPAR $\alpha$  for viability.

## 4 | DISCUSSION

Extracellular acidosis is a hallmark of the TME and has recently been assigned key roles in driving cancer aggressiveness.<sup>2,3</sup> Although it is well known that cell growth under long-term extracellular acidosis elicits widespread metabolic changes,<sup>2,3,20-23</sup> the mechanisms driving this are essentially unstudied. It should also be pointed out that, while, consistent with previous studies, we use the term *acid-adapted*, it is highly likely that the acidosis-driven event is a selection for those cancer cells that are able to survive the harsh acidic conditions. This is suggested from work from us and others<sup>7,38</sup> in which acid-adapted cells are returned to physiological pH, but a full understanding of the question will require DNA sequencing to study the genetic identity of the populations before and after acid exposure.

The key finding of our work is that acid-adapted cancer cells sustain growth at least in part through FA uptake and accumulation in LDs, stimulating a PPAR $\alpha$ -driven increase in mitochondrial and peroxisomal  $\beta$ -oxidation capacity (Figure 5I).

Exposure to acidic pH<sub>e</sub> will initially acidify pH<sub>i</sub> as a consequence of the increased inward driving force for H<sup>+</sup>.<sup>22</sup> The resulting pH<sub>i</sub> will depend on the balance between net acid influx, production and -efflux. To maintain pH<sub>i</sub> despite a substantial increase in the inward-directed driving force for H<sup>+</sup>, cells can increase net acid extrusion and/or reduce net acid production. We show here that both strategies are employed by cancer cells growing under acidic conditions. Acid-adapted cancer cells showed a markedly increased pH<sub>i</sub> as measured at physiological pH<sub>e</sub>, while they remained modestly acidic at acidic pH<sub>e</sub>. Consistent with this, acid-adapted cells showed increased expression of net acid extruding transporters. The specific transporters upregulated differed between cell types, emphasizing that the acidic microenvironment selects for the phenotype of increased acid extrusion, rather than for specific molecular targets. Interestingly, the Na<sup>+</sup>-HCO<sub>3</sub><sup>-</sup>-cotransporter NBCn1 (SLC4A7) was upregulated in all acid-adapted cells, suggesting the existence of pervasive regulatory mechanisms driving its upregulation at acidic pH<sub>e</sub>. This is particularly relevant given the importance of NBCn1 for mammary tumor pH regulation and tumor growth *in vivo* and the known links between this transporter and human mammary cancer.<sup>26,39</sup>

Consistent with earlier reports,<sup>21-23</sup> acid adaptation was associated with a shift toward oxidative metabolism. Remarkably however, the reserve glycolytic capacity revealed upon blocking mitochondrial activity was strongly increased in AA cells, suggesting that acidic stress increased metabolic flexibility. Given that already the first steps of glycolysis are potently inhibited by acidic pH<sub>i</sub>,<sup>2,19</sup> we reasoned that other substrates than glucose would be needed to supply OXPHOS in acid-adapted cells. Opportunistic nutrient acquisition, including scavenging of extracellular lipids followed by their accumulation in LDs, is characteristic of many cancer cells.<sup>33</sup> In line with this and with previous work,<sup>9</sup> we showed that cellular TAG and LD accumulation were increased in acid-adapted cells. The FA profile determined by shotgun lipidomics, and the lack of upregulation of enzymes associated with lipid synthesis such as FAS, are most consistent with the lipids being obtained directly from the extracellular environment. Although several SLC27 (FATP) family lipid uptake transporters were upregulated at mRNA level (Tables S1 and S2), we found no evidence (unpublished data) for involvement of these transporters, nor of CD36, previously suggested to mediate FA uptake in acid-adapted cells.<sup>9</sup> In fact, CD36 expression is very low in most cell types (eg, [www.proteinatlas.org](http://www.proteinatlas.org)), and was not detectable in Panc-1 or MDA-MB-231 cells (Tables S1 and S2). Mechanisms of transport of lipids across membranes remain widely debated.<sup>40</sup> However, given the pK<sub>a</sub> values of long-chain FAs, it is clear that at pH<sub>e</sub> 6.5, a much greater fraction of such FAs will be protonated and therefore un-ionized, allowing passage across the membrane by rapid flip-flop down their concentration gradient.<sup>41,42</sup> Thus, while we cannot exclude a partial role for lipid transport proteins, we propose that this elegantly simple biophysical mechanism is an early event initiating metabolic changes when pH<sub>e</sub> decreases. A possible additional lipid scavenging mechanism is macropinocytosis followed by autophagy, known to be upregulated in cancer cells by extracellular acidosis (Figure 5I).<sup>43,44</sup>

TAGs are released from LDs as FAs by direct adipose triglyceride lipase (ATGL)-mediated lipolysis and/or by lipophagy<sup>45</sup> (Figure 5I). Given that ATGL (*PNPLA2*) was upregulated only in Panc-1-AA cells (Figures 3A and S6) and that the autophagic machinery is, as noted above, upregulated by extracellular acidosis,<sup>43,44</sup> it seems likely that both mechanisms are involved in the acid-adapted cells. The FAs are subsequently utilized through  $\beta$ -oxidation in mitochondria and peroxisomes, followed by entry as acetyl-CoA into TCA cycle and OXPHOS. Consistent with this, we found that acid-adapted cancer cells exhibited increased mitochondrial and peroxisomal  $\beta$ -oxidation volume and increased expression of mitochondrial and peroxisomal enzymes important for lipid uptake and oxidation. How the OXPHOS efficiency of the elongated mitochondria of the acid adapted cells compares to that of control cells remains to be studied, however, mitochondrial elongation has been associated with increased OXPHOS efficiency and protection against mitophagy.<sup>32</sup> Analysis of transcription factor binding site enrichment and upregulation identified PPAR $\alpha$  as a candidate transcription factor contributing to the acid adaptation-induced metabolic changes. Incorporation of imported FAs into TAGs in LDs followed by their ATGL-mediated hydrolysis elicits FA-induced PPAR $\alpha$  stimulation.<sup>33</sup> This is a dual effect of the release of FAs which are direct PPAR $\alpha$  ligands, and ATGL-mediated activation of Sirtuin1, which activates peroxisome proliferator-activated receptor- $\gamma$ -coactivator-1 $\alpha$  (PGC-1 $\alpha$ ) and binds directly to PPAR $\alpha$ , facilitating its interaction with PGC-1 $\alpha$  and transcription of PGC-1 $\alpha$ /PPAR $\alpha$  target genes.<sup>46</sup> Upregulated PPAR $\alpha$  targets included key mitochondrial and peroxisomal drivers of lipid import and  $\beta$ -oxidation, PPAR $\alpha$  transcriptional activity was increased in acid-adapted cells, and PPAR $\alpha$  inhibition selectively reduced viability of acid-adapted cancer cells. Collectively this suggests that activation of PPAR $\alpha$  as a consequence of increased FA import is a key element of the metabolic changes occurring in cancer cells in acidic environments. While not necessarily protumorigenic in humans,<sup>47</sup> PPAR $\alpha$  signaling has been implicated in driving cancer cell proliferation, at least in part via transcriptional upregulation of CPTs.<sup>48</sup> Also in congruence with our findings, SIRT1 activity was previously implicated in acidosis-induced metabolic changes.<sup>49</sup> Further, the zinc transporter SLC39A10 (*ZIP10*) was one of the most highly upregulated genes in AA cells (Tables S1 and S2). Zinc is strictly required for PPAR $\alpha$  activity and increases PPAR $\alpha$  expression,<sup>50</sup> and thus *ZIP10* upregulation may be another adaptive mechanism facilitating lipid-based metabolism in acidic tumor niches. Finally, acid-induced upregulation of *TXNIP* was fully ablated by a specific PPAR $\alpha$  antagonist. Given the known inhibition of glucose uptake by *TXNIP*,<sup>51</sup> we suggest that *TXNIP* upregulation contributes to the PPAR $\alpha$ -induced metabolic shift by limiting glucose uptake.

It is worth noting that acidosis and hypoxia partially overlap in tumors.<sup>4,5</sup> The present work and work of others showing a shift toward mitochondrial metabolism in cancer cells under acidosis raise the question of what happens to these cells if they also become hypoxic. Recent work has suggested that breast cancer cells subjected to both conditions undergo a transition to a Warburg phenotype,<sup>52</sup> however, this would lead to rapid glucose depletion and select for alternative ways of obtaining nutrients, for example, by scavenging or

entosis,<sup>53</sup> pointing to potential new therapeutic strategies for targeting such cells.

In conclusion, cancer cells growing in an acidic microenvironment exhibit upregulation of net acid extrusion, attenuated glycolytic acid production, and increased FA uptake. This phenotype is associated with upregulation of peroxisomal and mitochondrial lipid import and  $\beta$ -oxidation capacity but maintenance of a high glycolytic reserve capacity, suggesting that a key trait acquired is increased metabolic flexibility. This metabolic rewiring is at least in part driven by PPAR $\alpha$  activation, and acid-adapted cancer cells accordingly exhibit increased sensitivity to PPAR $\alpha$  inhibition.

## AUTHOR CONTRIBUTIONS

Stine F. Pedersen, Michala G. Rolver, Elena Pedraz-Cuesta, Kenji Maeda and Albin Sandelin developed the concept. Michala G. Rolver established and performed Seahorse measurements, transient transfection, dual luciferase assay, mitochondrial quantification, and cellular agonist/antagonist treatment. Nanditha S. Prasad and Signe Kramer performed the live imaging of pH<sub>i</sub>. Michala G. Rolver, Muthulakshmi Ponniah, Line Elingaard-Larsen and Nanditha S. Prasad performed the IF analysis. SDS-PAGE and Western blotting were performed by Michala G. Rolver, Muthulakshmi Ponniah, Nanditha S. Prasad, Julie Schnipper, Signe Kramer, and Elena Pedraz-Cuesta. Elena Pedraz-Cuesta performed BrdU analyses. Luis A. Pardo and Stine F. Pedersen performed mitochondrial imaging analyses. Shotgun lipidomics were performed by Lya K. K. Holland and Kenji Maeda, and bioinformatics by Jiayi Yao, Albin Sandelin and Bin Liu. Figures were prepared by Michala G. Rolver with inputs from all authors. Michala G. Rolver and Stine F. Pedersen wrote the manuscript, with inputs and comments from all co-authors. All authors have read and approved the final version of the manuscript. The work reported in the paper has been performed by the authors, unless clearly specified in the text.

## ACKNOWLEDGEMENTS

The authors gratefully acknowledge the excellent technical assistance of Katrine Franklin Mark, Mette Flinck and Maria R. Mejlhart, and contribution of Shruti Gaggari in initial pilot experiments for this work. We also thank Lipidomics Core Facility at the Danish Cancer Society Research Center for providing access to instruments and materials.

## FUNDING INFORMATION

This work was supported by the Danish Cancer Society (Albin Sandelin, Stine F. Pedersen, #A12359), the Novo Nordisk Foundation (Albin Sandelin, Stine F. Pedersen, #NNF19OC0058262), Independent Research Fund Denmark (Stine F. Pedersen, #0135-00139B), Independent Research Fund Denmark (Kenji Maeda, #6108-00542B), Danish Cancer Society (Kenji Maeda, #R124-A7929-15-S2) and a BIO Elite PhD scholarship from the Department of Biology, University of Copenhagen, to Michala G. Rolver.



## CONFLICT OF INTEREST

The authors declare no conflict of interest.

**DATA AVAILABILITY STATEMENT**

RNA-seq data is deposited at GEO with accession number GSE152345. Further details and other data that support the findings of this study are available from the corresponding author upon request.

**ORCID**

Michala G. Rolver  <https://orcid.org/0000-0002-4139-1218>  
 Albin Sandelin  <https://orcid.org/0000-0002-7109-7378>  
 Stine Falsig Pedersen  <https://orcid.org/0000-0002-3044-7714>

**TWITTER**

Albin Sandelin  @albin\_san  
 Stine Falsig Pedersen  @StineFPedersen1

**REFERENCES**

1. Swietach P. What is pH regulation, and why do cancer cells need it? *Cancer Metastasis Rev.* 2019;38:5-15.
2. Boedtker E, Pedersen SF. The acidic tumor microenvironment as a driver of cancer. *Annu Rev Physiol.* 2020;82:103-126.
3. Corbet C, Feron O. Tumour acidosis: from the passenger to the driver's seat. *Nat Rev Cancer.* 2017;17:577-593.
4. Rohani N, Hao L, Alexis MS, et al. Acidification of tumor at stromal boundaries drives transcriptome alterations associated with aggressive phenotypes. *Cancer Res.* 2019;79:1952-1966.
5. Helmlinger G, Yuan F, Dellian M, Jain RK. Interstitial pH and pO<sub>2</sub> gradients in solid tumors in vivo: high-resolution measurements reveal a lack of correlation. *Nat Med.* 1997;3:177-182.
6. Martínez-Zaguilán R, Seftor EA, Seftor RE, Chu YW, Gillies RJ, Hendrix MJ. Acidic pH enhances the invasive behavior of human melanoma cells. *Clin Exp Metastasis.* 1996;14:176-186.
7. Moellering RE, Black KC, Krishnamurty C, et al. Acid treatment of melanoma cells selects for invasive phenotypes. *Clin Exp Metastasis.* 2008;25:411-425.
8. Zhu S, Zhou HY, Deng SC, et al. ASIC1 and ASIC3 contribute to acidity-induced EMT of pancreatic cancer through activating Ca<sup>2+</sup>/RhoA pathway. *Cell Death Dis.* 2017;8:e2806.
9. Corbet C, Bastien E, Santiago de Jesus JP, et al. TGFβ<sub>2</sub>-induced formation of lipid droplets supports acidosis-driven EMT and the metastatic spreading of cancer cells. *Nat Commun.* 2020;11:454.
10. Robey IF, Baggett BK, Kirkpatrick ND, et al. Bicarbonate increases tumor pH and inhibits spontaneous metastases. *Cancer Res.* 2009;69:2260-2268.
11. Flinck M, Kramer SH, Schnipper J, Andersen AP, Pedersen SF. The acid-base transport proteins NHE1 and NBCn1 regulate cell cycle progression in human breast cancer cells. *Cell Cycle.* 2018;17:1056-1067.
12. Flinck M, Kramer SH, Pedersen SF. Roles of pH in control of cell proliferation. *Acta Physiol (Oxf).* 2018;223:e13068.
13. Pouyssegur J, Sardet C, Franchi A, L'Allemain G, Paris S. A specific mutation abolishing Na<sup>+</sup>/H<sup>+</sup> antiport activity in hamster fibroblasts precludes growth at neutral and acidic pH. *Proc Natl Acad Sci USA.* 1984;81:4833-4837.
14. Putney LK, Barber DL. Na-H exchange-dependent increase in intracellular pH times G<sub>2</sub>/M entry and transition. *J Biol Chem.* 2003;278:44645-44649.
15. Boron WF. Regulation of intracellular pH. *Adv Physiol Educ.* 2004;28:160-179.
16. Boedtker E, Moreira JM, Mele M, et al. Contribution of Na<sup>+</sup>, HCO<sub>3</sub><sup>-</sup>-cotransport to cellular pH control in human breast cancer: a role for the breast cancer susceptibility locus NBCn1 (SLC4A7). *Int J Cancer.* 2013;132:1288-1299.

17. Malinda RR, Zeeberg K, Sharku PC, et al. TGFbeta signaling increases net acid extrusion, proliferation and invasion in Panc-1 pancreatic cancer cells: SMAD4 dependence and link to Merlin/NF2 signaling. *Front Oncol.* 2020;10:687.
18. Payen VL, Mina E, Van Hée VF, Porporato PE, Sonveaux P. Monocarboxylate transporters in cancer. *Mol Metab.* 2020;33:48-66.
19. Trivedi B, Danforth WH. Effect of pH on the kinetics of frog muscle phosphofruktokinase 1. *J Biol Chem.* 1966;241:4110-4112.
20. Corbet C, Pinto A, Martherus R, Santiago de Jesus JP, Polet F, Feron O. Acidosis drives the reprogramming of fatty acid metabolism in cancer cells through changes in mitochondrial and histone acetylation. *Cell Metab.* 2016;24:311-323.
21. LaMonte G, Tang X, Chen JL, et al. Acidosis induces reprogramming of cellular metabolism to mitigate oxidative stress. *Cancer Metab.* 2013;1:23.
22. Michl J, Wang Y, Monterisi S, et al. CRISPR-Cas9 screen identifies oxidative phosphorylation as essential for cancer cell survival at low extracellular pH. *Cell Rep.* 2022;38:110493.
23. Wu H, Ying M, Hu X. Lactic acidosis switches cancer cells from aerobic glycolysis back to dominant oxidative phosphorylation. *Oncotarget.* 2016;7:40621-40629.
24. Wilde BR, Ye Z, Lim TY, Ayer DE. Cellular acidosis triggers human MondoA transcriptional activity by driving mitochondrial ATP production. *Elife.* 2019;8.
25. Yao J, Czaplinska D, Ialchina R, et al. Cancer cell acid adaptation gene expression response is correlated to tumor-specific tissue expression profiles and patient survival. *Cancers (Basel).* 2020;12(8):2183.
26. Andersen AP, Samsøe-Petersen J, Oerbo EK, et al. The net acid extruders NHE1, NBCn1 and MCT4 promote mammary tumor growth through distinct but overlapping mechanisms. *Int J Cancer.* 2018;142:2529-2542.
27. Ritchie ME, Phipson B, Wu D, et al. Limma powers differential expression analyses for RNA-sequencing and microarray studies. *Nucleic Acids Res.* 2015;43:e47.
28. Nielsen I, Vidas Olsen A, Dicroce-Giacobini J, et al. Comprehensive evaluation of a quantitative shotgun lipidomics platform for mammalian sample analysis on a high-resolution mass spectrometer. *J Am Soc Mass Spectrom.* 2020;31:894-907.
29. Kwon AT, Arenillas DJ, Worsley HR, Wasserman WW. oPOSSUM-3: advanced analysis of regulatory motif over-representation across genes or ChIP-seq datasets. *G3 (Bethesda).* 2012;2:987-1002.
30. Fornes O, Castro-Mondragon JA, Khan A, et al. JASPAR 2020: update of the open-access database of transcription factor binding profiles. *Nucleic Acids Res.* 2020;48:D87-D92.
31. Pike Winer LS, Wu M. Rapid analysis of glycolytic and oxidative substrate flux of cancer cells in a microplate. *PLoS One.* 2014;9:e109916-e.
32. Pedersen SF, Flinck M, Pardo LA. The interplay between dysregulated ion transport and mitochondrial architecture as a dangerous liaison in cancer. *Int J Mol Sci.* 2021;22:1-27.
33. Petan T. Lipid droplets in cancer. *Rev Physiol Biochem Pharmacol.* 2020;1-34.
34. Wanders RJA, Waterham HR, Ferdinandusse S. Metabolic interplay between peroxisomes and other subcellular organelles including mitochondria and the endoplasmic reticulum. *Front Cell Dev Biol.* 2016;3.
35. Kersten S, Stienstra R. The role and regulation of the peroxisome proliferator activated receptor alpha in human liver. *Biochimie.* 2017;136:75-84.
36. Pettersen IKN, Tusubira D, Ashrafi H, et al. Upregulated PDK4 expression is a sensitive marker of increased fatty acid oxidation. *Mitochondrion.* 2019;49:97-110.
37. Bougarne N, Weyers B, Desmet SJ, et al. Molecular actions of PPAR-alpha in lipid metabolism and inflammation. *Endocr Rev.* 2018;39:760-802.



38. Czaplinska D. Crosstalk between tumor acidosis, p53, and extracellular matrix regulates pancreatic cancer aggressiveness. *Int J Cancer*. 2022;1-16.
39. Lee S, Axelsen TV, Andersen AP, Vahl P, Pedersen SF, Boedtkjer E. Disrupting Na<sup>+</sup>, HCO<sub>3</sub><sup>-</sup>-cotransporter NBCn1 (Slc4a7) delays murine breast cancer development. *Oncogene*. 2016;35:2112-2122.
40. Kamp F, Hamilton JA. How fatty acids of different chain length enter and leave cells by free diffusion. *Prostaglandins Leukot Essent Fatty Acids*. 2006;75:149-159.
41. Kamp F, Hamilton JA. pH gradients across phospholipid membranes caused by fast flip-flop of un-ionized fatty acids. *Proc Natl Acad Sci U S A*. 1992;89:11367-11370.
42. Spector AA. Influence of pH of the medium on free fatty acid utilization by isolated mammalian cells. *J Lipid Res*. 1969;10:207-215.
43. Marino ML, Pellegrini P, Di Lernia G, et al. Autophagy is a protective mechanism for human melanoma cells under acidic stress. *J Biol Chem*. 2012;287:30664-30676.
44. Wojtkowiak JW, Rothberg JM, Kumar V, et al. Chronic autophagy is a cellular adaptation to tumor acidic pH microenvironments. *Cancer Res*. 2012;72:3938-3947.
45. Schott MB, Rozeveld CN, Weller SG, McNiven MA. Lipophagy at a glance. *J Cell Sci*. 2022;135:1-7.
46. Khan SA, Sathyanarayan A, Mashek MT, Ong KT, Wollaston-Hayden EE, Mashek DG. ATGL-catalyzed lipolysis regulates SIRT1 to control PGC-1alpha/PPAR-alpha signaling. *Diabetes*. 2015;64:418-426.
47. Corton JC, Peters JM, Klaunig JE. The PPARalpha-dependent rodent liver tumor response is not relevant to humans: addressing misconceptions. *Arch Toxicol*. 2018;92:83-119.
48. Chen Y, Wang Y, Huang Y, et al. PPAR $\alpha$  regulates tumor cell proliferation and senescence via a novel target gene carnitine palmitoyltransferase 1C. *Carcinogenesis*. 2017;38:474-483.
49. Corbet C, Draoui N, Polet F, et al. The SIRT1/HIF2alpha axis drives reductive glutamine metabolism under chronic acidosis and alters tumor response to therapy. *Cancer Res*. 2014;74:5507-5519.
50. Reiterer G, Toborek M, Hennig B. Peroxisome proliferator activated receptors alpha and gamma require zinc for their anti-inflammatory properties in porcine vascular endothelial cells. *J Nutr*. 2004;134:1711-1715.
51. Parikh H, Carlsson E, Chutkow WA, et al. TXNIP regulates peripheral glucose metabolism in humans. *PLoS Med*. 2007;4:e158.
52. Damaghi M, West J, Robertson-Tessi M, et al. The harsh microenvironment in early breast cancer selects for a Warburg phenotype. *Proc Natl Acad Sci U S A*. 2021;118:1-10.
53. Finicle BT, Jayashankar V, Edinger AL. Nutrient scavenging in cancer. *Nat Rev Cancer*. 2018;18:619-633.

## SUPPORTING INFORMATION

Additional supporting information can be found online in the Supporting Information section at the end of this article.

**How to cite this article:** Rolver MG, Holland LKK, Ponniah M, et al. Chronic acidosis rewires cancer cell metabolism through PPAR $\alpha$  signaling. *Int J Cancer*. 2023;152(8):1668-1684. doi:[10.1002/ijc.34404](https://doi.org/10.1002/ijc.34404)